




# Phase evolution and thermoelectric performance of $\text{Cu}_2\text{SnS}_3$

Wen Gu<sup>1,2</sup>, Bingguo Liu<sup>1,\*</sup>, Shunzi Li<sup>1</sup>, Baofu Hu<sup>1</sup>, Jian Xu<sup>1</sup>, Jian Wang<sup>1,\*</sup> , and Baoli Du<sup>1,2</sup>

<sup>1</sup>School of Physics and Electronic Information Engineering, Henan Polytechnic University, Jiaozuo 454000, China

<sup>2</sup>Henan Key Laboratory of Materials on Deep-Earth Engineering, Henan Polytechnic University, Jiaozuo 454000, China

**Received:** 17 February 2023

**Accepted:** 24 April 2023

**Published online:**  
5 May 2023

© The Author(s), under exclusive licence to Springer Science+Business Media, LLC, part of Springer Nature 2023

## ABSTRACT

$\text{Cu}_2\text{SnS}_3$  (CTS), as a potential thermoelectric (TE) material, the electrical and thermal transport properties are heavily determined by its original phase structure and the following phase evolution upon heating. Unlike previous studies that induced CTS phase transition by doping, this study used mechanical alloying powder as the precursor and successfully prepared phase-pure cubic (c-) and monoclinic (m-) CTS samples, as well as two-phase mixed samples with different percentage composition of c-CTS and m-CTS, by simply adjusting the hot pressing temperature. Firstly, phase structures of hot-pressed specimens were determined and confirmed by XRD refinement, SEM, TEM, and Raman spectroscopy. Secondly, thermodynamic property was analyzed by DSC analysis, and phase evolution was detailed by analyzing specimens quenched at various temperatures. Then, the electrical and thermal transport properties were measured up to 500 °C, and were correlated with phase evolution analyzed above. Benefiting from cationic disorder, a maximum  $zT$  of 0.42 at 500 °C was achieved in c-CTS samples hot-pressed at 575 °C. The phase evolution of CTS was comprehensively investigated by using high-quality samples. The results indicate that phase transition is the potential mechanism for the doping effect in most studies, providing some guidance for improving the performance of environmentally friendly TE sulfides.

## 1 Introduction

Thermoelectric (TE) conversion technology, with TE materials as the core, is widely used in space vehicle energy supply [1], automotive exhaust waste heat generation, computer hardware cooling, and temperature differential electric cold water dispenser

[2, 3]. In addition, it is helpful to improve the efficiency of fossil energy and promote the process of replacing traditional energy sources with new ones. Thermoelectric sulfides, with the advantages of non-toxicity, low cost and abundant content, are excellent TE candidates for power generating operating at medium temperature. Among them, Cu-Sb-S

Address correspondence to E-mail: lbg@hpu.edu.cn; jianwang@hpu.edu.cn

compounds are considered as a promising class of TE materials due to their compositional and structural diversity, including  $\text{Cu}_{12}\text{Sb}_4\text{S}_{13}$ ,  $\text{Cu}_3\text{SbS}_4$  and  $\text{Cu}_3\text{SbS}_3$  [4–6].  $\text{Cu}_3\text{SbS}_4$  has a tetragonal-coordinated zinc blende structure,  $\text{Cu}_{12}\text{Sb}_4\text{S}_{13}$  tetrahedra has a complex cubic structure, and  $\text{Cu}_3\text{SbS}_3$  has a variety of orthorhombic, monoclinic, and cubic structures [5, 6]. It is worth mentioning that  $\text{Cu}_{12}\text{Sb}_4\text{S}_{13}$  shows a  $zT$  of 1, and the Fe doped cubic  $\text{Cu}_3\text{SbS}_3$  sample reaches a  $zT$  of 0.62 at 350 °C [7]. However, the element Sb is rare and toxic. It is nominally trivalent in  $\text{Cu}_3\text{SbS}_3$ , and contains lone pair of electrons that make the structure unstable [7]. Sn, adjacent to Sb in the periodic table, has one less electron in the outermost layer, can all be bonded in the analog Cu–Sn–S compounds. Moreover, Sn is more environmentally friendly and cheaper than Sb. Therefore, some researchers shift their focus from Cu–Sb–S system to Cu–Sn–S compounds by replacing Sb with Sn.

$\text{Cu}_2\text{SnS}_3$  (CTS) compound is an abundant, environmentally friendly, non-toxic p-type semiconductor material [8]. It is widely studied in fields of solar cells, photocatalysis, gas sensing, antibacterial and others [9–12]. Similarly, silicon-based compounds have also attracted widespread attention due to their excellent TE conversion efficiency [13]. Especially for SiGe compounds and their nanostructured materials, the SiGe nanowires could significantly improve their power factor and thus enhanced the TE performance due to the energy filtering effect introduced by defects and defects produced in preparation process [14]. However, a major drawback of silicon-based TE materials is their high lattice thermal conductivity [13]. In contrast, CTS has lower lattice thermal conductivity in the moderate temperature range, making it a promising TE material [8]. It is reported that CTS has various crystalline forms, such as monoclinic (m-CTS; SG: CC), cubic (c-CTS; SG: F-43m) and tetragonal (t-CTS; SG: I-42m) [15]. These crystalline types were identified as ordered, disordered, and pseudo-ordered structures, respectively [16–19]. Although no consensus reached among researchers on the process conditions for the synthesis of multiple crystalline forms of CTS, it is generally accepted that CTS has a tetragonal structure below 400 °C, and a mixture of cubic (c-CTS) and monoclinic (m-CTS) crystalline forms above 400 °C. Monoclinic crystalline systems are dominative above 500 °C [18, 20]. There are 24 atoms in the unit cell of monoclinic structure with all atoms (Cu, Sn, and S) occupy the 4a Wyckoff position

[21–23]. In the cubic structure [23], Cu and Sn occupy the 4a position (with Cu accounting for 66.7%, Sn for 33.3%), and S occupies the 4c Wyckoff position. Four cations of Cu and Sn bond to a S anion in tetrahedral fashion in both cubic and monoclinic structures [23].

CTS has a three-dimensional conducting network, consisting of hybridized 3d (Cu)-3p (S) orbitals and S–S 3p orbitals in the valence band, which gives it good electrical transport properties. High density of states contributes to the excellent p-type TE properties of CTS too [23, 24]. It is worth mentioning that Sn is nominally tetravalent in CTS, compared to trivalent of Sb in Cu–Sb–S system. No lone pair of electrons were formed on Sn sites, after the bonding of all outmost layer electrons to anion S, which may lower the anharmonicity of the lattice vibration, and reduce the suppression effect of thermal conductivity [25]. Interesting, CTS has comparably low thermal conductivity with Cu–Sb–S system, due to its special order–disorder structure. It shows a thermal conductivity of  $0.75 \text{ W m}^{-1} \text{ K}^{-1}$  at 500 °C in ordered monoclinic phase [26], and much lower in disordered cubic structure ( $0.39 \text{ W m}^{-1} \text{ K}^{-1}$  at 500 °C) [27]. All the above suggests that CTS has good prospects for medium temperature TE applications [28].

Most researches are related to the transition metal doping which facilitates the phase transition from a cation-ordered low-symmetry structure (m-CTS) to disordered high-symmetry structures (t-CTS and c-CTS), and improves the electrical or thermal transport performances or both. Large amount of acceptor doping is capable of transforming the unit cell of CTS, resulting in a superlattice structure in the c-direction, which enhances the effects of phonon scattering, reduces lattice thermal conductivity  $\kappa_{\text{latt}}$ , and optimizes the electrical transport property through energy band engineering and carrier concentration optimization [29]. Shen et al. observed the transformation from m-CTS into cubic and tetragonal mixed phase structure in Zn-doped samples, which shows a  $zT$  of 0.58 at 450 °C [8]. Tan et al. obtained a  $zT$  of 0.50 at 427 °C in m-CTS by doping In, and the thermal conductivity was below  $1.0 \text{ W m}^{-1} \text{ K}^{-1}$  [30]. Zhao et al. further increased  $zT$  to 0.84 at 450 °C by cobalt doping at Sn site. This approach also yielded an ultra-low lattice thermal conductivity of about  $0.3\text{--}0.4 \text{ W m}^{-1} \text{ K}^{-1}$  [26]. So far, the highest  $zT$  of about 0.9 ( $T > 427 \text{ °C}$ ) was obtained by co-doping of Co and Sb at Sn site [31]. These reports all confirm the efficacy of transforming of CTS from ordered

monoclinic phase to disordered cubic and tetragonal phases by Sn site acceptor doping.

Although many studies have been carried out on CTS, there are still some basic problems that have not yet been solved. For example, multiple crystalline forms of CTS have similar X-ray diffraction patterns [9], so more analytic techniques are needed to assist the determination of the crystalline forms. Although the idea of combination use of Raman, XRD, TEM were proposed to determine the proportion of each phase when multiple crystal forms coexist [20], the details and applicability of the available techniques are not comprehensive enough, and more methods are needed to be developed. Secondly, phase transition process of CTS from cubic to monoclinic phase and its influences are not yet clear. For examples, no references mentioned the influences of decomposition and accompanying impurities generation on the TE property in the process of measurement. In other word, the influences of the composition and degree of the phase transition on the electrical and thermal transport properties are rarely reported. In this study, both phase-pure cubic and monoclinic CTS, as well as a series of mixed phase samples were successfully obtained by hot pressing temperature adjustment, rather than Sn site doping used in most of the references. The phases of the samples were confirmed and analyzed by combined use of XRD, Raman, TEM, et al. The phase transition and impurities generation with temperature, and their influences on electrical and thermal transport properties were revealed in the DSC and TE performance measurements.

## 2 Experimental details

$\text{Cu}_2\text{SnS}_3$  was synthesized from commercial powders of copper (99.9%), 99.8% tin, and 99.5% sulfur (Aladdin). Mechanical alloying was used to obtain precursor for hot pressing. Raw powders were placed in a stainless steel ball-milling tank together with stainless steel balls. The ball-powder ratio was kept at 20:1. The samples were ball milled at 450 rpm for 24 h under low-pressure Ar atmosphere (QM1SP2, Nanjing University). Then, the obtained powders from mechanical alloying were loaded into graphite die and hot-pressed at 550, 575, 600, 625 and 650 °C for 1 h (OTF-1200X-VHP4, Kejing Hefei, China). The densities of all samples are above 94% of the theoretical value.

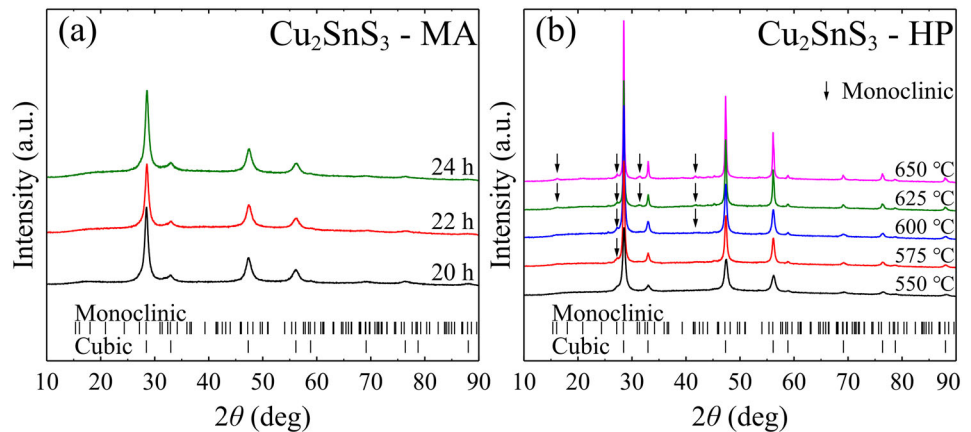
The phase structure of samples were characterized by X-ray diffraction (XRD, Cu  $K\alpha$ , X'Pert Pro-Panalytical, The Netherlands). Rietveld refinement was performed on the CTS series samples using Maud software. Raman spectra were collected using a micro Raman spectrometer (Raman, inVia, Renishaw, UK). Scanning electron microscopy (SEM, Merlin Compact, Germany) was used to observe the microscopic morphology of fresh fracture surface of the samples. Selected area electron diffraction (SAED) images were collected with a transmission electron microscope (TEM, JEOL2100, Japan). The thermal stability of the samples was analyzed by differential scanning calorimetry (DSC, Q20, TA Instruments, New Castle, DE, USA) under a flowing  $\text{N}_2$  atmosphere, with a temperature ramp rate of 5 K/min. The Hall coefficient was measured with a commercial instrument (HL5500, Ecoopia, Korea) with a magnetic field of 0.53 T. The resistivity and Seebeck coefficient of the samples were measured with a commercial instrument (CTA-3, Cryoall, China) under  $\text{N}_2$  atmosphere. The thermal diffusivity  $D$  of the material was measured by a laser flash method (LFA-457, Netzsch, Germany), and then the total thermal conductivity was calculated according to the equation  $\kappa = DC_P d$ , where the heat capacity  $C_P$  was calculated by the Dulong–Petit law, and the density  $d$  was calculated by mass and volume.

## 3 Result and discussion

### 3.1 Composition, phase structure and morphology

XRD results for powders obtained by ball milling are shown in Fig. 1a. No apparent impurity peaks were observed in all samples, well in agreement with the standard cubic structure of CTS (SG: F-43 m). It means shortening the milling time is still possible for obtaining c-CTS powders. Figure 1b shows the XRD patterns of bulk samples obtained after hot-pressing at 550, 575, 600, 625 and 650 °C for 1 h, using the powder mechanical-alloyed of 24 h. In CTS-550 sample, only the diffraction peaks of c-CTS were observed, and no obvious impurities peaks of other crystal forms of CTS and binary sulfides were observed, suggesting a much purer cubic phase

**Fig. 1** Room temperature X-ray diffraction patterns of CTS samples **a** powers mechanical alloyed (MA) for 20 h, 22 h and 24 h, and **b** pellets hot-pressed (HP) at 550, 575, 600, 625 and 650 °C for 1 h



sample was obtained than that reported in references [32].

From 575 °C, with the increase of sintering temperature, the characteristic Bragg peaks (16.12°, 27.2°, 31.4° and 41.7°) of monoclinic phase (m-CTS) appears, and their intensities increase gradually, and the samples gradually transit from disordered cubic phase to monoclinic phase. When sintered at 650 °C, the obtained sample has a phase-pure m-CTS structure, completely consistent with the standard m-CTS (SG: Cc) structure. Between 550 and 650 °C, samples are mixtures of monoclinic and cubic phases, free of binary sulfide impurities. The above results indicate that it is possible to adjust the percentage composition of m-CTS and c-CTS by only adjusting the sintering temperature, using mechanical alloyed powder as precursor. It is worth noting that the X-ray diffractograms of the three crystal structures of CTS (cubic, monoclinic, and tetragonal) are very similar [9]. So the purity of the above-stated phase-pure samples obtained at 550 and 650 °C are actually in doubt, and further analysis is needed to verify the results, and determine the percentage composition of m-CTS and c-CTS in the mixed samples.

The XRD patterns of samples hot-pressed at different temperatures were quantitatively analyzed by Rietveld refinement method and the results were shown in Fig. 2. The CTS-550 sample displays a disordered cubic phase, and no traces of other phases including monoclinic and tetragonal CTS were detected. So the co-existence of multiple CTS phases at 550 °C can be ruled out currently. When sintered at 575 °C, the monoclinic phase appears. Hence, the CTS-575 sample is a mixture of cubic and monoclinic phases. And small amount of monoclinic phase (11.27%) is embedded in the matrix cubic phase

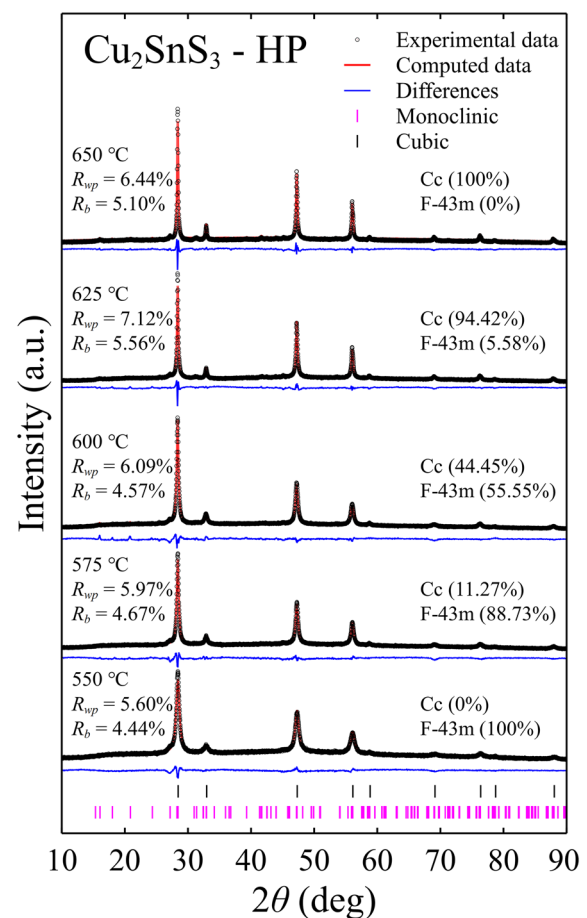


**Fig. 2** The Rietveld refinements of the XRD patterns of CTS samples hot-pressed at different temperatures. Quantitative analysis of the phases is also included

(88.73%). The proportion of the monoclinic phase increases continuously with the increase of sintering temperature, whereas the content of the cubic phase decreases proportionally. While the CTS-600 is roughly a mixture of half cubic and half monoclinic

structure, the CTS-625 sample is dominated by monoclinic phase, only 5.58% cubic phase was figured out. Further increase the hot-pressing temperature to 650 °C, the CTS-650 sample becomes 100% monoclinic, free of cubic phase completely. No tetragonal phase was detected in any of the samples obtained in this work. Also the small value of  $R_{wp}$  indicates that the simulated X-ray diffraction spectra are in good agreement with the experimental ones.

Though XRD is convenient and powerful to characterize the average structure of powders, it is less sensitive to reveal the local structure on scale of grain size when multiple phases with similar XRD patterns are mixed together, just the case of CTS. So, SAED patterns of individual grains were collected under TEM. As shown in Fig. 3a, c, e, the Debye–Scherrer rings of the CTS-550 sample coincide with the three strongest Bragg-peaks of the XRD pattern of the cubic phase, which confirms that only cubic phase was included in the sample sintered at 550 °C. The SEAD of the monoclinic CTS-650 sample displays not only the three rings corresponding to the three strongest Bragg peaks of the monoclinic structure, but also the

unique (1 3 0) and (− 3 1 2) plane diffraction rings of the structure. No rings corresponding to other phases were detected. For CTS-600 sample, the SEAD result includes a (1 1 1) plane diffraction ring unique to the cubic phase. At the same time, it contains the (1 3 0) and (− 3 1 2) plane diffraction rings unique to the monoclinic phase, which confirms the coexistence of the two phases.

The SEM images of fresh fracture surfaces of the CTS samples (b) CTS-550, (d) CTS-600, and (f) CTS-650 are shown in Fig. 3. Due to the ball-milling process and relatively low hot-pressing temperature, all samples have dense microstructure with sub-micrometer grains. When hot pressing at 550 °C, the average grain size is the smallest, ranging from 20 to 100 nm. The average grain size grows slightly with the increase of hot-pressing temperature. For the monoclinic CTS-650 sample hot-pressed at 650 °C, it reaches approximately 100 nm, still much finer than the samples prepared by other methods, which would have strong influences on the thermal transport properties discussed below.

Though the phase-pure structures of CTS-550, and CTS-650 were determined by the methods described above, they still may contain traces of impurities according to reports in the literature [32]. Raman scattering is sensitive to local atomic bonding and vibration. So, it is highly applicable to distinguish between the subtle bonding environment difference within cubic and monoclinic structures of CTS. As shown in Fig. 4, the CTS-550 sample has obvious Raman peaks around 287  $\text{cm}^{-1}$  and 345  $\text{cm}^{-1}$ , which is consistent with the Raman mode of the cubic phase reported in references [33, 34]. Also, broad shoulder associated with cubic structure was also observed around 330  $\text{cm}^{-1}$ , which is caused by the vibration of atomic bonds between copper and tin, the broadening of which is linked to the confinement effect of phonons [12]. For CTS-650 sample, there are clear Raman peaks around 290 and 352  $\text{cm}^{-1}$ , in good agreement with the mode of monoclinic structure reported in the literature [16]. When sintered at 575 °C, 600 °C and 625 °C, both Raman peaks shift away from the position of the pure cubic (287 and 345  $\text{cm}^{-1}$ ) and monoclinic phases (290 and 352  $\text{cm}^{-1}$ ), and lie in between them.

Due to composition deviation caused by synthesis method [12], different combination of Raman modes, for example, 300 and 350 [35], 303 and 365 [36], and 299 and 351  $\text{cm}^{-1}$  [37] for cubic structure were also

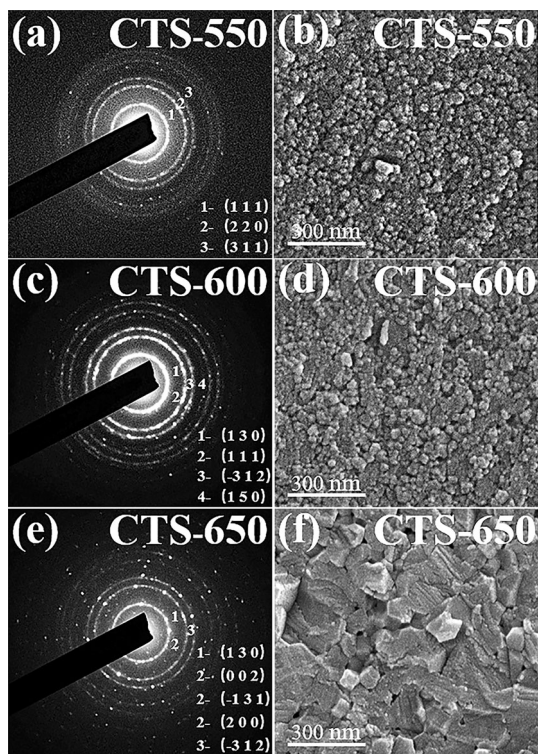


**Fig. 3** The selected area electron diffraction (SAED) images collected under TEM, and the SEM images of freshly fractured surfaces of CTS-550 (a, b), CTS-600 (c, d) and CTS-650 (e, f) samples

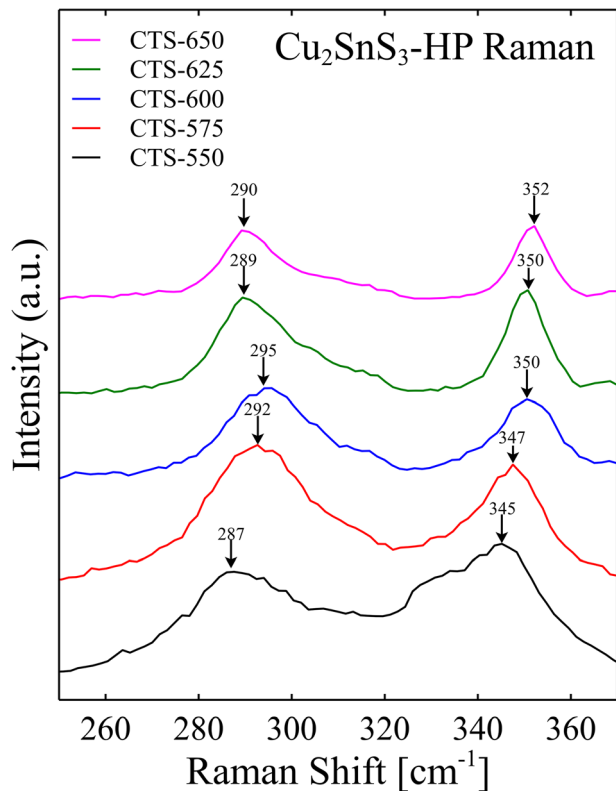


**Fig. 4** Raman spectra of CTS samples hot-pressed at 550, 575, 600, 625, and 650 °C

reported in literature, which reflects the complexity of the atomic bond vibration of the cubic phase of CTS, as well as the complexity of the composition and structure caused by the random occupancy of cations. Similar different results were also reported for monoclinic structure [38, 39]. So, the relative position and intensity of the two main peaks were used to further discuss the Raman results.

Firstly, the distance of the two main Raman peaks of all samples were calculated and shown in Fig. 5a. In contrast to the monotonous increase of the distance from cubic to monoclinic phases reported by Oliva et al. the distance of the Raman peaks decreases first and then increases as the increase of the sintering temperature from 550 to 650 °C. From pure cubic CTS-550 to CTS-575 with a small amount of monoclinic phase, the distance between the two main peaks decreases from 58 to 55 cm<sup>-1</sup>, and remained almost unchanged when moving further to the CTS-600 sample with 44.45% of monoclinic phase. This result suggests that the actual phase structure and composition of the samples with lower concentration of monoclinic phase prepared in this work are

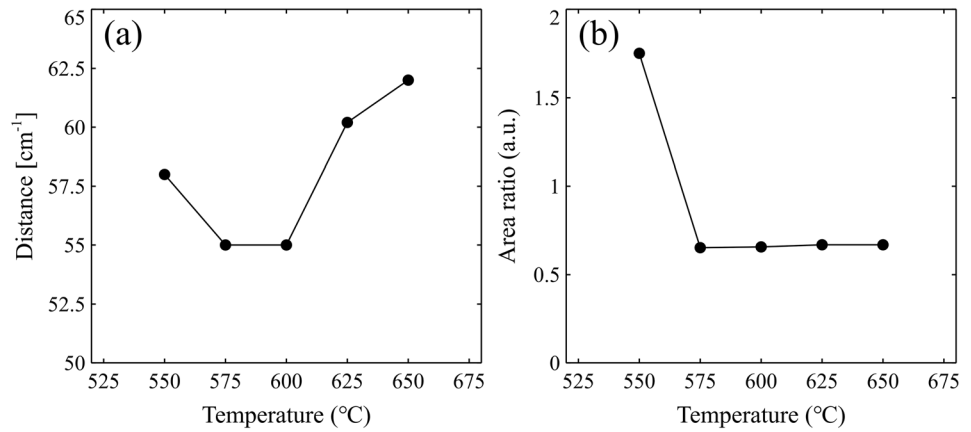
different from those reported by Olivia et al. [20]. Actually, a small amount of Mo<sub>2.06</sub>S<sub>3</sub> and Cu<sub>4</sub>Sn<sub>7</sub>S<sub>16</sub> impurities are present in the nominally pure cubic sample reported in the reference [20]. Moreover, abnormal strong background noise or protrusion around 27° were observed in XRD pattern in CTS-550 sample. Though no peak were assigned at this position both by XRD and refinement programs, the abnormality suggests the possibility of the existence of traces of unidentified impurity in CTS-550 sample.

From sample CTS-600 to CTS-650, the distance increases continually with the increase of the content of monoclinic phase, in good agreement with the results reported by Olivia et al. [20]. So, it is safe to state that the distance is positively related to the content of monoclinic phase in the monoclinic-phase-rich samples, though the sample reported in reference is a mixture of 69.7% cubic phase and 30.3% monoclinic phase. Moreover, the relation between the distance and the phase structure in the monoclinic-phase-poor samples is much complex, and strongly depends on the kinds and concentration of impurities.

Secondly, the relative intensity of (or the area under) the two main peaks were qualitatively correlated to the ratio between cubic and monoclinic phases. Figure 5b shows the ratio of area II (under peak 310–360 cm<sup>-1</sup>) to area I (under peak 260–310 cm<sup>-1</sup>). Except CTS-550 sample, the area ratio keeps unchanged with the increase of percentage composition of monoclinic phase from CTS-575 to CTS-650 samples, completely different from the monotonous increase reported by Olivia et al. [20]. It is worth noting that our sample spans a broad range from CTS-575 with 11.27% of monoclinic phase to CTS-650 with pure-phase monoclinic structure, while the samples from reference have 30.3% monoclinic phase in maximum. For pure cubic CTS-550 sample, the broad shoulder around 330 cm<sup>-1</sup> contributes a lot to the area II and pushed the ratio to as high as 1.79, much bigger than the average value of 0.66 for other samples with monoclinic phase.

Above all, high-purity CTS samples with cubic and monoclinic structures were successfully achieved and confirmed by XRD, TEM, and Raman analysis. By only adjusting the hot-pressing temperature, a series of samples with different cubic to monoclinic phase ratio were obtained, laying the foundation for determining their thermodynamic property and outlining the influences of possible phase transition and

**Fig. 5** **a** Distance between the two main Raman modes, **b** ratio of the peak area of the two main Raman modes of the CTS samples



decomposition on electrical and thermal properties when used as TE materials.

### 3.2 Thermodynamic properties

DSC analysis was conducted to determine their thermodynamic properties of CTS-550, CTS-600 and CTS-650 samples. As shown in Fig. 6, the CTS-650 sample with monoclinic structure exhibits much better thermal stability than the other two samples. It just has two apparent endothermic steps observed around 320 and 430 °C, with the characteristic of an irreversible reaction of glass transition. Taking into account of relatively low hot-pressing temperature, it is possible that part of the ball-milling powder with amorphous or semi-crystalline characteristics is fused

into the bulk material, and transforms into crystalline states during the DSC heating process. No reactions can be seen in the cooling process.

In contrast, the CTS-550 sample with cubic structure shows a strong endothermic peak and a strong exothermic peak at 303 and 424 °C, with the second one associating with the phase transition from cubic to monoclinic structure. The CTS-600 sample exhibits a significant peak at 338 °C, far away from the value of the cubic to monoclinic phase transition around 400 °C reported in the reference [40] and 424 °C of CTS-550 sample.

To shed light on the unknown DSC peaks and underlying phase transition, CTS-550 specimens were quenched at 350 and 500 °C respectively, to determine their phase structures by XRD (Fig. 7) and Raman (Fig. 8a) spectroscopy analysis. Same measurements were also conducted on CTS-600 sample quenched at 500 °C (Fig. 8b).

As shown in Fig. 7, XRD of CTS-550 specimen quenched at 350 °C indicates that the DSC peak at 303 °C is closely related to the decomposition of the cubic phase, supporting by the appearing of peaks assigned to binary impurities, CuS and SnS, and S<sub>8</sub> appeared. Tetragonal CTS was also observed in the specimen quenched at 350 °C, though the main phase keeps intact as cubic. Simultaneously, as shown in Fig. 8a, Raman peak at 333/328 cm<sup>-1</sup> associated to tetragonal structure was observed in CTS-550 specimens quenched both at 350 and 500 °C, with the second main peak shifted from 345 cm<sup>-1</sup> for specimens unquenched, and quenched at 350 °C, to 340 cm<sup>-1</sup> for specimen quenched at 500 °C. Interestingly, the cubic phase dominates the matrix even after quenched at 500 °C, far beyond the cubic to monoclinic phase transition temperature 424 °C. This

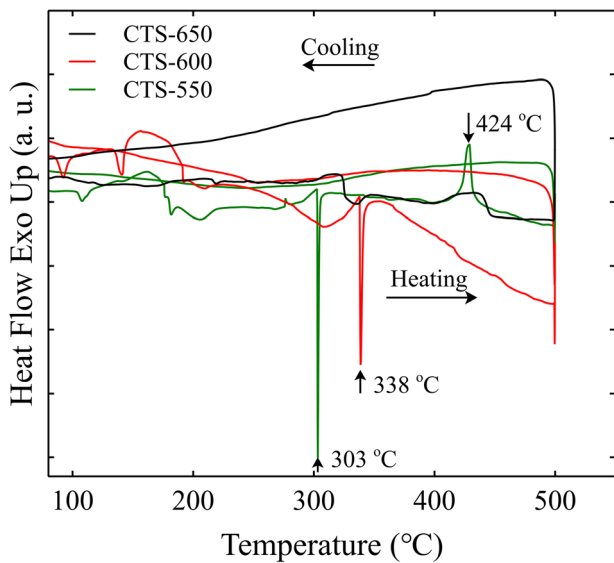


**Fig. 6** DSC curves of CTS-550, CTS-600 and CTS-650 samples

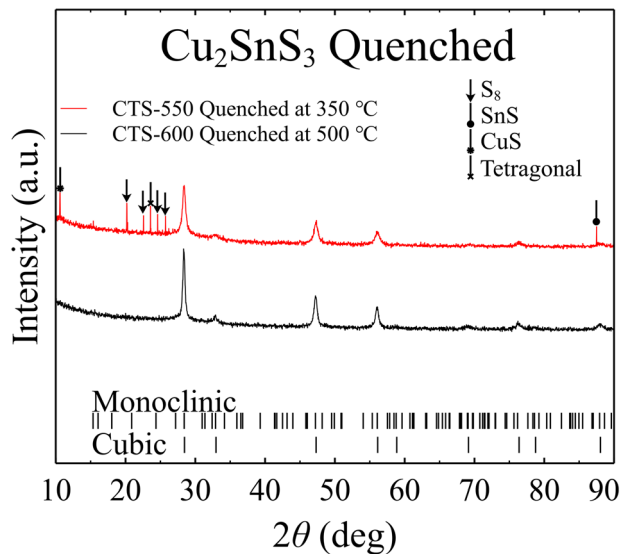


**Fig. 7** X-ray diffraction patterns of CTS-550 sample quenched at 350 °C and CTS-600 sample quenched at 500 °C

suggests that the phase transition is strongly kinetically controlled and explains the existence and achievability of monoclinic phase (high temperature structure) after cooling down to room temperature.

For CTS-600 sample with half cubic and half monoclinic phase, binary impurity SnS was observed in XRD after heated to 500 °C and quenched, along with the Raman peak at  $351\text{ cm}^{-1}$  shifted to  $347\text{ cm}^{-1}$ , similar with the trend shown in the Raman spectrum of CTS-550 sample. No Raman peak assigned to tetragonal phase was detected. So the

degree of the phase transition, from cubic to both monoclinic and tetragonal phases, is strongly correlated to the concertation of the monoclinic phase, 44.45% of which is capable of suppressing the cubic to tetragonal phase transitions in heating process.

Actually, strong heat flow turbulence appears at much lower temperature before the first strong DSC peak at 303 °C in CTS-550 sample. Moreover, two apparent weak peaks and one downward step were observed in CTS-600 sample. Both indicates the complexity of the phase evolution during DSC measurement. So it is important to keep in mind that the complexity of phase transition and decomposition process upon heating, when trying to clarify the influences of phase structure on electrical and thermal transport properties.

### 3.3 Electrical transport property

Figure 9 shows the temperature dependence of (a) electrical resistivity and (b) Seebeck coefficient for the different CTS samples. For comparison, data of reference samples is also included. At room temperature, the resistivities of all CTS samples are strongly correlated to the phase structure or hot-pressing temperature. The CTS-550 sample with cubic phase structure displays the lowest values of resistivity, while the resistivity of the CTS-650 sample with monoclinic phase is close to the highest value of all samples.

**Fig. 8** **a** Raman spectra of CTS-550 samples quenched at 350 and 500 °C, and **b** CTS-600 sample quenched at 500 °C. The original Raman spectra of the both samples were also added for comparison

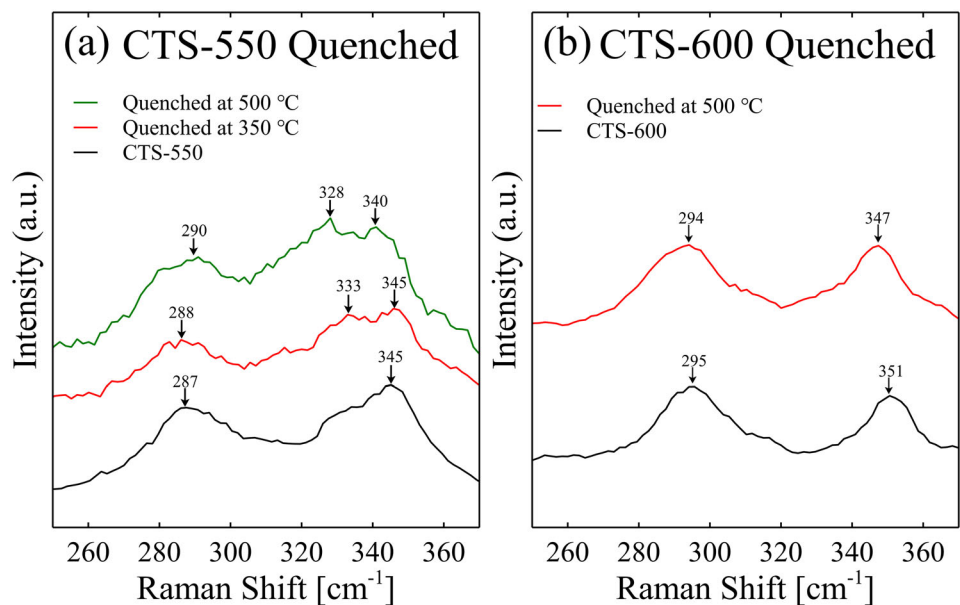
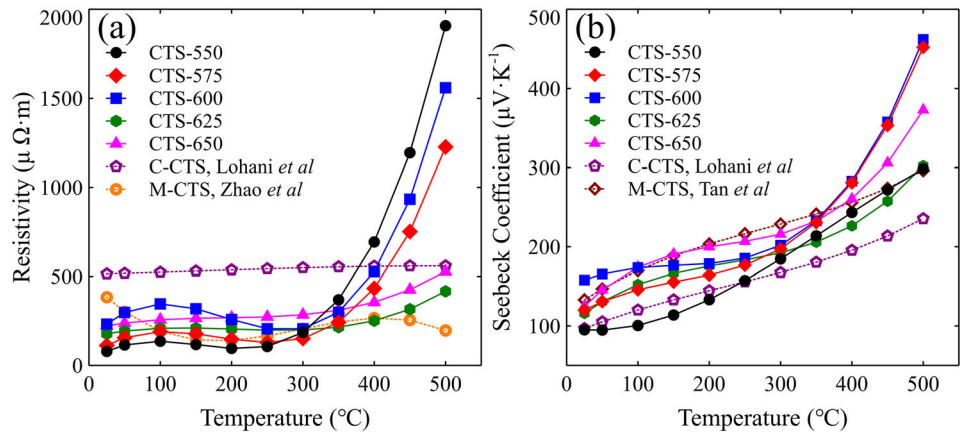




**Fig. 9** Temperature dependence of **a** electrical resistivity and **b** Seebeck coefficient for CTS samples. Reference samples were also included for comparison



Taking into account the characteristics of cation disorder and finer grain size (lower hot pressing temperature), the cubic CTS-550 sample should process a higher resistivity or a small carrier mobility at least, because both characteristics contribute negatively to the transport of charge carriers. However, according to the results of the Hall test measurement results shown in Table 1, both the carrier concentration and mobility of the CTS-550 sample are higher than those of the CTS-650 sample. So, the electronic band structure discrepancy between cubic and monoclinic structure, including the value of band gap and the valence band edge fine structure, plays a decisive role in determining the electrical transport property. This deduction is well consistent with the band structure calculation in references [41]. With narrow band gap compared with monoclinic structure, energy of the cubic CTS-550 sample exhibits a lower resistivity despite the characteristics of cation disorder, which lays the foundation for many of the researches related to the transition metal doping. It facilitates transition from the cation-ordered m-CTS to the disordered c-CTS, and improves the electrical or/and thermal transport properties [42].

However, for samples with coexistence of both cubic and monoclinic phases, the resistivity is strongly correlated to both the phase structure and

the microstructure. Sample CTS-575 has a higher resistivity than cubic CTS-550 due to its larger carrier concentration but much lower carrier mobility (less than half of that of CTS-550). For sample CTS-660 with half cubic and half monoclinic phases, its resistivity is the highest among all samples. So extra carrier scattering aroused by grain boundaries and the associated defects between the two phases dominates the charge carrier transport, and results in a low mobility and a resistivity as high as 232.3 μΩ m.

According the characteristic of temperature dependence of resistivity, a strong correlation between resistivity and phase structure is observed. Below 260 °C, samples can be divided into two groups, one is the CTS-625 and CTS-650 samples with a nearly constant resistivity (Group I), the other is CTS-550, CTS-575, and CTS-600 samples (Group II), which firstly show a slight increase then a decrease in resistivity. Compared with Group II samples, Group I samples have high proportion of monoclinic phase confirmed by XRD refinement and rather stable thermal stability shown in DSC analysis. Also, the room resistivity of the Group I samples was similar to the study by Zhao et al. [26]. Notably, the complex phase transition in cubic-phase-rich samples (Group II), manifested in DSC measurement, plays an important role in determining the electrical transport properties,

**Table 1** Room-temperature hall coefficients, carrier concentrations and mobilities of different CTS samples

Samples	$R_H$ (cm <sup>3</sup> C <sup>-1</sup> )	$n$ (× 10 <sup>20</sup> cm <sup>-3</sup> )	$\mu_H$ (cm <sup>2</sup> V <sup>-1</sup> S <sup>-1</sup> )
CTS-550	0.053	1.2	6.7
CTS-575	0.035	1.8	3.2
CTS-600	0.11	0.58	4.7
CTS-625	0.11	0.57	6.1
CTS-650	0.13	0.47	6.0

and may even dominates the temperature dependence of resistivity as shown in this case. Above 260 °C, the resistivities of the Group I samples slowly increased with the increase of temperature., while these of Group II samples increase dramatically. According to the DSC results, no significant changes occurred in the Group I samples. So, Group I samples exhibits the intrinsic electrical transport property of monoclinic CTS. However, decomposition and phase transition were observed in Group II samples, which mainly contributes to the sharp increase of resistivities above 260 °C. Microcracks were discovered under SEM in Group II samples, which manifests the influences of phase evolution on both phase structure and microstructure upon heating up to 260 °C. Based on the above analysis, it is reasonable to deduce that the variation of resistivity reported by Zhao et al. was closely related to phase transition or decomposition during measurement. We conjectured that Zhao's monoclinic sample may contain certain amount of cubic phase, or/and other CTS phases, or/and binary sulfides impurities [26]. Moreover, the resistivity of the cubic CTS-550 sample is not only lower than that of Lohani et al. [27], but also displays rather different temperature dependence. So, there must be less phase evolution in Lohani's sample during measurement. In one word, the original phase structure and the phase transition upon heating are the two main factors for resistivity. Original structure and phase evolution aside, it would be pointless to discuss the underlying physics of doping effects in most of the researches, though quiet good  $zT$ s were achieved.

As shown in Fig. 9b, Seebeck coefficients of all specimens are positive, reflecting the p-type form of transport. As expected, samples with high resistivity have higher Seebeck coefficients and vice versa around room temperature, but deviate the law of thumb at high temperature. For monoclinic CTS-650 sample, the Seebeck coefficient ranges from 185 to 380  $\mu\text{V K}^{-1}$ , higher than the values of 133–296  $\mu\text{V K}^{-1}$  for m-CTS reported by Tan et al. [30]. The Group II samples (CTS-575 and CTS-600) with coexistence of cubic and monoclinic phase exhibit the highest Seebeck coefficients above 400  $\mu\text{V K}^{-1}$  around 500 °C. However, the phase-pure cubic CTS-550 within the same group has the lowest Seebeck coefficient at room temperature, due to its narrow band gap and high carrier concentration (low resistivity). Though, its Seebeck coefficient increase with increase of

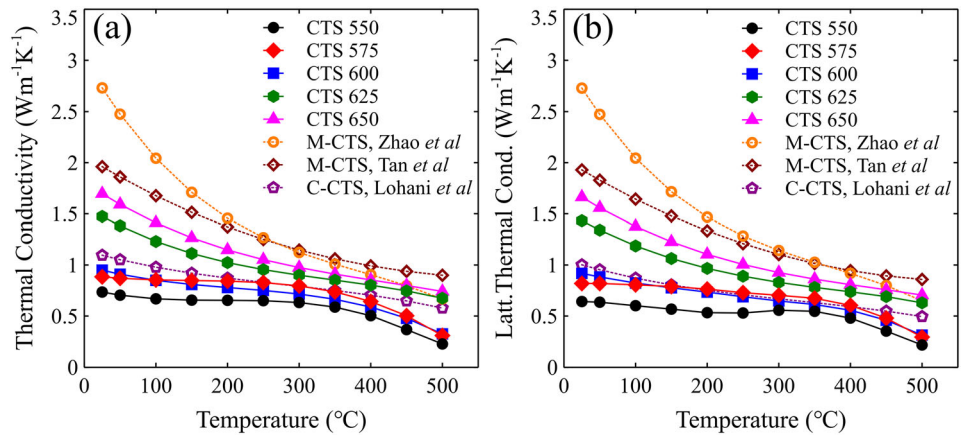
temperature as other samples, above 300 °C, the grow of Seebeck coefficient loses momentum compared other Group II samples, and a lowest value is obtained at 500 °C, in contrast to its highest resistivity. Considering the similar DSC behavior of Group II samples, we conjectured that the coexistence of two phases or the associated grain boundaries works as energy barrier and effectively scatters low-energy charge selectively, and optimizes the Seebeck coefficient through the energy filtering effect. As a whole, the Seebeck coefficient of sample CTS-550 falls in the range of 95–300  $\mu\text{V K}^{-1}$ , similar to these (97–235  $\mu\text{V K}^{-1}$ ) reported by Lohani et al. [29] below 250 °C. At elevated temperature, though the values of this study fall short of expectation because of its high resistivity, they are still higher than the results reported in reference (300 vs. 235  $\mu\text{V K}^{-1}$  at 500 °C) [29]. These results firmly demonstrates that phase evolution, including phase transition between different CTS structures and decomposition of the specimens into binary sulfides, cannot be neglected in determining Seebeck coefficient, just as in the case of resistivity [43].

### 3.4 Thermal conductivity and figure-of-merit $zT$

As shown in Fig. 10a, the monoclinic CTS-650 sample has highest thermal conductivity over the whole temperature range, ranging from 1.70 to 0.74  $\text{Wm}^{-1}\text{K}^{-1}$ . But it is much lower than that of other diamond-like structure compounds, such as  $\text{CuFeS}_2$  (5.9  $\text{Wm}^{-1}\text{K}^{-1}$ ) [44] and  $\text{CuInTe}_2$  (6.0  $\text{Wm}^{-1}\text{K}^{-1}$ ) [45], benefiting from its low-symmetry monoclinic structure [31]. Moreover, it is less than the values of m-CTS reported by Zhao [26], Tan [30]. The cubic CTS-550 sample has a thermal conductivity of 0.74  $\text{Wm}^{-1}\text{K}^{-1}$  at room temperature and 0.23  $\text{Wm}^{-1}\text{K}^{-1}$  at 500 °C, both of which are much less than that of c-CTS prepared by Lohani et al. [29], though the specimen of this study has a higher relative density of 94%.

Apart from the potential phase structure discrepancy in samples prepared by different research groups, the low thermal conductivity of the samples of this study is closely related to the fine microstructure, resulted from the combination use of ball-milling and low temperature hot-pressing. In order to gain insight into the mechanism of thermal transport property, the lattice thermal conductivity

**Fig. 10** Temperature dependence of **a** thermal conductivity and **b** lattice thermal conductivity for CTS samples. For comparison, data of reference samples were also included



$\kappa_{latt}$  was estimated by subtracting the electronic thermal conductivity  $\kappa_{carr}$  from the total thermal conductivity  $\kappa$ , where  $\kappa_{carr}$  was calculated according to the Wiedemann-Franz law ( $\kappa_{carr} = L\sigma T$ ).

As shown in Fig. 10b, the lattice thermal conductivity of all samples decreases with increasing temperature, indicating the dominance of phonon U-scattering process. Over the whole temperature range, the cubic CTS-550 sample has lower thermal conductivity than that of monoclinic CTS-650 sample. Two factors are accounted the large discrepancy. One is the cation disorder in cubic structure. Though cubic structure exhibits a high degree of symmetry compared with monoclinic structure, the cation disorder introduces extra phonon scattering mechanism and effectively limits the lattice thermal conductivity to a value that corresponds to the minimum possible, where the phonon mean free path equals the interatomic distance. The other factor is the finer microstructure in CTS-550 sample due to its low hot-pressing temperature.

For samples with coexistence of both cubic and monoclinic phases, the thermal conductivity falls in between phase-pure cubic CTS-550 and monoclinic CTS-650 samples. This suggests that, though the grain boundary associating with coexistence of two phases may play a role in phonon transport, the intrinsic cation disorder and micro-structure dominates the thermal transport properties in all samples.

Similar with resistivity, samples can be divided into the same two groups based on detailed characteristic of temperature dependence above 350 °C. The group I samples, including samples CTS-625 and CTS-650, have lattice thermal conductivity decreasing smoothly with increasing temperature over the whole temperature, which indicates that the main process is

U scattering, without obvious influence of other factors. However, the lattice thermal conductivity of group II samples (including CTS-550, CTS-575 and CTS-600) decreases rapidly after 350 °C, obviously deviating from the trend below 350 °C. Combined with the DSC and resistivity analysis, it is safe to deduce that phase evolution, or the increase of density of grain boundary and the following micro-cracks, is the underlying physics of the accelerating decrease of lattice thermal conductivity above 350 °C.

The TE figure of merit  $zT$  is calculated based on the values of resistivity, Seebeck coefficient and thermal conductivity. Figure 11 shows the temperature dependence of  $zT$  of all CTS samples. The  $zT$ s of all samples increase rapidly with increasing temperature, but are relatively small at room temperature. A maximum  $zT$  of 0.16 is reached in cubic CTS-550 sample at 500 °C. It is rather low compared with the  $zT$  of 0.38 at the same temperature prepared by Lohani et al. [29], which is mainly hindered by high resistivity. Also, due to the decomposition and cubic to monoclinic phase transition, an abnormal change of  $zT$  was discovered in cubic CTS-550 sample.

The maximum  $zT$  0.27 of the monoclinic CTS-650 sample is reached at 500 °C, comparable to the  $zT \sim 0.26$  at 500 °C reported in the literature [30]. Please keep in mind that this is the result achieved in a non-doped CTS samples, optimization of carrier concentration by doping will definitely enhance the  $zT$  by doping, which has been confirmed in Zn doping [8], In doping [30] and Co and Sb co-doping [31] samples.

The maximum  $zT$  0.42 among all the samples was achieved in CTS-575 sample with coexistence of cubic and monoclinic phases. So, future researches should not be confined to phase-pure CTS samples,

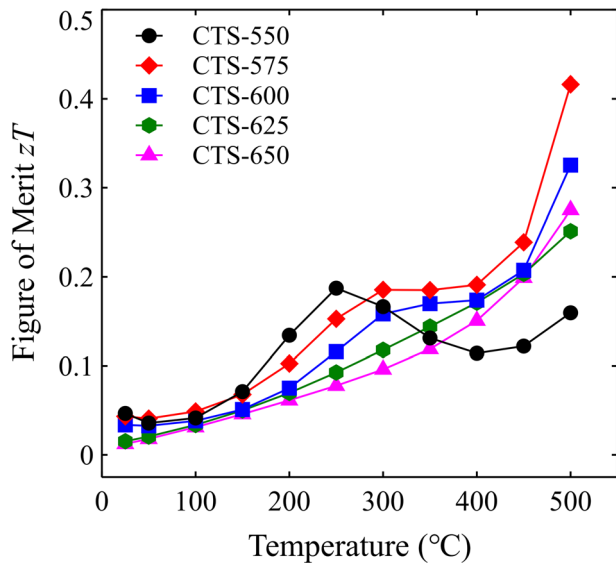


**Fig. 11** Figure-of-merit  $zT$  for CTS

suitable two-phase pairing or grain boundary environment may be another way to obtain high  $zT$ , as long as the influences of phase structure can be tailored properly.

## 4 Conclusions

To shed light on the influences of phase evolution on TE properties in CTS, the phase-pure cubic and monoclinic samples, and two-phase mixed samples with different percentage of c-CTS and m-CTS were synthesized by using mechanical alloyed power as precursor and by only regulating the hot-pressing temperature. By combined use of XRD refinement, Raman, SEM, and TEM, the phase structures of all samples were confirmed and compared with results reported in references. DSC analysis indicates that the monoclinic CTS-650 sample exhibits much better thermal stability than cubic CTS-550 and CTS-600 samples with mixed phase. The cubic CTS-550 sample has a tendency to decompose to binary sulfides at low temperature, and transform to monoclinic structure at higher temperature, though the cubic phase still dominating the matrix even after 500 °C. The above discovery indicates that the phase transition between cubic to monoclinic phase is strongly kinetically controlled and explains the availability of high-temperature monoclinic phase at room temperature. The electrical and thermal transport properties of CTS were closely related to the original phase

structure of CTS after hot pressing and the phase transition during heating. All samples can be divided into two distinct groups, Group I with monoclinic phase in dominance, and Group II with high percentage of cubic phase. Benefiting from the disordered structure of cations, a maximum  $zT$  of 0.42 at 500 °C was obtained in c-CTS sample. This study clarified the phase transition of undoped CTS samples after heating and established the relationship between phase transition and TE performance. Simultaneously, an explanation of the underlying mechanism of doping effects in most researches was proposed based on phase evolution.

## Author contributions

All authors contributed to the study conception and design. Material preparation, data collection and analysis were performed by WG, SL, BH and JX. BD, JW, and BL are responsible for writing—reviewing and editing manuscript and funding acquisition.

## Funding

This work was supported by the National Science Foundation of China (Grant Nos. 51772076, 51802083), the Science Foundation of Henan Province (Grant Nos. 222300420448, 182300410248, 182300410193), and Science & Technology Projects of Henan Province (Grant Nos. 202102210247). BD also acknowledges the financial support from Marie Curie International Incoming Fellowship of the European Community Human Potential Program under Contract no. PIIFR-GA-2013-913847 (Return Phase).

## Data availability

All data that support the findings of this study are included within the article.

## Declarations

**Conflict of interest** The authors declare no conflict of interest.

## References

1. C. Candolfi, S.E. Oualid, D. Ibrahim, S. Misra, O.E. Hamouli, A. Léon, A. Dauscher, P. Masschelein, P. Gall, P. Gougeon, C. Semprimoschnig, B. Lenoir, *CEAS Space J.* **13**, 325–340 (2021)
2. S. Wiriyasart, C. Hommalee, R. Prurapark, A. Srichat, P. Naphon, *Phase II, Case Stud. Ther. Eng.* **15**, 100520 (2019).
3. A. Çağlar, *Appl. Ther. Eng.* **149**, 822–828 (2019).
4. C. Zhu, Q. Chen, H. Ming, X. Qin, Y. Yang, J. Zhang, D. Peng, T. Chen, D. Li, Y. Kawazoe, *ACS Appl. Mater. Interf.* **13**, 25092–25101 (2021).
5. K. Chen, C. Di Paola, B.L. Du, R.Z. Zhang, S. Laricchia, N. Bonini, C. Weber, I. Abrahams, H.X. Yan, M. Reece, *J. Mater. Chem. C* **6**, 8546–8552 (2018).
6. J. Wang, T. Wang, J.J. Zhang, B.G. Liu, L.J. Wang, W. Gu, B.F. Hu, J. Xu, B.L. Du, *J. Solid State Chem.* **310**, 123014 (2022).
7. B. Du, R. Zhang, M. Liu, K. Chen, H. Zhang, M.J. Reece, *J. Mater. Chem. C* **7**, 394–404 (2019).
8. Y. Shen, C. Li, R. Huang, R. Tian, Y. Ye, L. Pan, K. Koumoto, R. Zhang, C. Wan, Y. Wang, *Sci. Rep.* **6**, 32501 (2016).
9. A.C. Lokhande, R.B.V. Chalapathy, M. He, E. Jo, M. Gang, S.A. Pawar, C.D. Lokhande, J.H. Kim, *Sol. Energy Mater. Sol. Cell* **153**, 84–107 (2016)
10. F. Chen, J. Zai, M. Xu, X. Qian, *J. Mater. Chem. A* **1**, 4316 (2013)
11. A.C. Lokhande, A.A. Yadav, J. Lee, M. He, S.J. Patil, V.C. Lokhande, C.D. Lokhande, J.H. Kim, *J. Alloy. Compd.* **709**, 92–103 (2017)
12. A.C. Lokhande, A. Shelke, P.T. Babar, J. Kim, D.J. Lee, I.C. Kim, C.D. Lokhande, J.H. Kim, *RCS Adv.* **7**, 33737–33744 (2017).
13. Y. Li, G. Wang, M. Akbari-Saatlu, M. Procek, H.H. Radamson, *Front. Mater.* **8**, 611078 (2021)
14. M. Noroozi, G. Jayakumar, K. Zahmatkesh, J. Lu, L. Hultman, M. Mensi, S. Marcinkevicius, B. Hamawandi, M.Y. Tafti, A.B. Erğül, Z. Ikonc, M.S. Toprak, H.H. Radamson, *ECS J. Solid State Sci. Technol.* **6**(9), Q114 (2017)
15. J. De Wild, E.V.C. Robert, B.E. Adib, D. Abou-Ras, P.J. Dale, *Sol. Energy Mater. Sol. Cell* **157**, 259–265 (2016)
16. D.M. Berg, R. Djemour, L. Gutay, S. Siebentritt, P.J. Dale, X. Fontane, V. Izquierdo-Roca, A. Perez-Rodriguez, *Appl. Phys. Lett.* **100**, 192103 (2012).
17. Y. Ben Smida, O. Oyewo, S. Ramaila, L. Mavuru, R. Marzouki, D.C. Onwudiwe, A.H. Hamzaoui, *J. Inorg. Organomet. Polym. Mater.* **32**, 4679–4693 (2022)
18. P. Zawadzki, L.L. Baranowski, H.W. Peng, E.S. Toberer, D.S. Ginley, W. Tumas, A. Zakutayev, S. Lany, *Appl. Phys. Lett.* **103**, 253902 (2013).
19. Z. Zhang, H.W. Zhao, Y.F. Wang, X.H. Hu, Y.N. Lyu, C.C. Cheng, L. Pan, C.H. Lu, *J. Alloy. Compd.* **780**, 618–625 (2019).
20. F. Oliva, L. Arqués, L. Acebo, M. Guc, Y. Sánchez, X. Alcobé, A. Pérez-Rodríguez, E. Saucedo, V. Izquierdo-Roca, *J. Mater. Chem. A* **5**, 23863–23871 (2017).
21. A.V. Postnikov, N.B.M. Amiri, *Phys. Status Solidi* **210**, 1332–1335 (2013)
22. Y.-T. Zhai, S. Chen, J.-H. Yang, H.-J. Xiang, X.-G. Gong, A. Walsh, J. Kang, S.-H. Wei, *Phys. Rev. B* **84**, 075213 (2011)
23. L. Xi, Y.B. Zhang, X.Y. Shi, J. Yang, X. Shi, L.D. Chen, W. Zhang, J. Yang, D.J. Singh, *Phys. Rev. B* **86**, 155201 (2012)
24. S. Thiruvenkadam, P. Sakthi, S. Prabhakaran, S. Chakravarty, V. Ganesan, A.L. Rajesh, *Phys. B* **538**, 8–12 (2018)
25. E.J. Skoug, D.T. Morelli, *Phys. Rev. Lett.* **107**, 235901 (2011).
26. H.W. Zhao, X.X. Xu, C. Li, R.M. Tian, R.Z. Zhang, R. Huang, Y.N. Lyu, D.X. Li, X.H. Hu, L. Pan, Y.F. Wang, *J. Mater. Chem. A* **5**, 23267–23275 (2017)
27. K. Lohani, C. Fanciulli, P. Scardi, *Materials* **15**, 712 (2022)
28. X. Xu, H. Zhao, X. Hu, L. Pan, C. Chen, D. Li, Y. Wang, *J. Alloy. Compd.* **728**, 701–708 (2017).
29. K. Lohani, H. Nautiyal, N. Ataollahi, K. Maji, E. Guilmeau, P. Scardi, *ACS Appl. Energy Mater.* **4**, 12604–12612 (2021).
30. Q. Tan, W. Sun, Z.L. Li, J.F. Li, *J. Alloy. Compd.* **672**, 558–563 (2016).
31. Y. Zhao, Y. Gu, P. Zhang, X. Hu, Y. Wang, P. Zong, L. Pan, Y. Lyu, K. Koumoto, *Sci. Technol. Adv. Mater.* **22**, 363–372 (2021).
32. K. Lohani, E. Isotta, N. Ataollahi, C. Fanciulli, A. Chiappini, P. Scardi, *J. Alloy. Compd.* **830**, 154604 (2020).
33. Y.C. Dong, J. He, X.R. Li, W.L. Zhou, Y. Chen, L. Sun, P.X. Yang, J.H. Chu, *Mater. Lett.* **160**, 468–471 (2015).
34. W. Wang, H.L. Shen, J.Z. Li, *Mater. Lett.* **111**, 5–8 (2013).
35. P.A. Fernandes, P.M.P. Salomé, A.F. da Cunha, *Phys. Status Solidi* **7**, 901–904 (2010)
36. E.L. Barbedo, P.H. Gonçalves, M.S. Lamoglia, A.M.P. Pontes, B.H. Bastos Kuffner, G.F. Gomes, G. Silva, *Mater. Res.* **24**, 0054 (2021).
37. L.L. Baranowski, K. McLaughlin, P. Zawadzki, S. Lany, A. Norman, H. Hempel, R. Eichberger, T. Unold, E.S. Toberer, A. Zakutayev, *Phys. Rev. Appl.* **4**, 044017 (2015).
38. M. He, A.C. Lokhande, I.Y. Kim, U.V. Ghorpade, M.P. Suryawanshi, J.H. Kim, *J. Alloy. Compd.* **701**, 901–908 (2017).
39. T. Raadik, M. Grossberg, J. Krustok, M. Kauk-Kuusik, A. Crovetto, R.B. Ettliger, O. Hansen, J. Schou, *Appl. Phys. Lett.* **110**(26), 261105 (2017)
40. E.A. Pogue, M. Goetter, A. Rockett, *Mater. Res. Soc. Adv.* **2**, 3181–3186 (2017).

41. A. Shigemi, T. Maeda, T. Wada, *Phys. Status Solidi B* **252**, 1230–1234 (2015)
42. H.T.T. Nguyen, V.S. Zakhvalinskii, T.T. Pham, N.T. Dang, T.V. Vu, E.A. Pilyuk, G.V. Rodriguez, *Mater. Res. Exp.* **6**, 055915 (2019).
43. C. Wang, Y.D. Chen, J. Jiang, R. Zhang, Y. Niu, T. Zhou, J.F. Xia, H.Q. Tian, J. Hu, P. Yang, *RSC Adv.* **7**, 16795–16800 (2017).
44. Y. Li, T. Zhang, Y. Qin, T. Day, G. Jeffrey Snyder, X. Shi, L. Chen, *J. Appl. Phys.* **116**, 203705 (2014).
45. R. Liu, L. Xi, H. Liu, X. Shi, W. Zhang, L. Chen, *Chem. Commun.* **48**, 3818–3820 (2012).

**Publisher's Note** Springer nature remains neutral with regard to jurisdictional claims in published maps and institutional affiliations.

Springer Nature or its licensor (e.g. a society or other partner) holds exclusive rights to this article under a publishing agreement with the author(s) or other rightsholder(s); author self-archiving of the accepted manuscript version of this article is solely governed by the terms of such publishing agreement and applicable law.